URTeC: 2457663

Physical Models for Inter-Well Interference in Shale Reservoirs: Relative Impacts of Fracture Hits and Matrix Permeability

Wei Yu*, Kan Wu, Lihua Zuo, Xiaosi Tan, Ruud Weijermars, Texas A&M University

Summary

The objective of this study is to develop physical models to quantitatively simulate the pressure response of well interference through fracture hits with complex geometries. Our study offers a model for an improved understanding of the influence of key reservoir and fracture properties on intensity of well interference, which may help field operators to further optimize the spacing of wells in a multi-well pad. We combine numerical, semi-analytical, and analytical model tools to identify, analyze, and visualize the inter-well interference process. Our analysis can account for complex non-planar fracture geometries using a semi-analytical model. The stimulated rock volume is visualized by an analytical streamline model. Three scenarios for well interference are investigated including interference through a single slanted fracture hit, multiple slanted fracture hits, and multiple complex fracture hits. For the first scenario, we examine the effects of connecting fracture conductivity, primary fracture conductivity, and matrix permeability on the pressure response of a shut-in well. For the second scenario, we vary the number of connecting fractures to investigate the impact on the pressure response of a shut-in well. For the last scenario, we use a complex fracture propagation model to generate non-planar fracture geometries with and without natural fractures. The semi-analytical model is used to evaluate the effect of both hydraulic and natural fractures on the pressure response of a shut-in well. The simulation results show that the pressure drop of the shut-in well increases with the increasing conductivity of connecting fractures and primary fractures and number of connecting fractures, while decreases with the increasing of matrix permeability. Furthermore, the pressure drop of the shut-in well through complex fracture hits without natural fractures is larger than that with natural fractures.

Introduction

Determination of the optimum well spacing is a key factor to improve the economic performance of unconventional oil and gas resources developed with multi-well pads. Tighter well spacing often results in well interference through complex connecting fractures, also known as fracture hits (Lawal et al. 2013; King and Valencia 2016). It is common to drill infill wells in a multi-well pad to effectively increase the stimulated area and maximize recovery (Safari et al. 2015). However, infill well drilling increases the risk of well interference. Ideally, the infill wells should have the minimum well interference with the existing wells (Ajani and Kelkar 2012). When the well spacing is much closer, the well interference is more frequent (Ajani and Kelkar 2012; Malpani et al. 2015; Kurtoglu and Salman 2015). The fracture hits can negatively affect well performance when damaging a well (Yaich et al. 2014; Malpani et al. 2015). Hence, a better understanding of well interference is fundamentally important for further well spacing optimization.

Well interference is a common phenomenon for both conventional and unconventional resource developments (King and Valencia 2016). It is expected to occur in any shale formation with the presence of the pre-existing natural fractures (Rimedio et al. 2015). The degree of well interference can be observed and quantified through the change of parent wells' performance when drilling offset wells (Ajani and Kelkar 2012; Yaich et al. 2014). The wells might show an increase in water production and an increase or decrease in oil or gas production (Lawal et al. 2013; Kurtoglu and Salman 2015). In addition, pressure testing on pad wells is often utilized to identify the well interference (Portis et al. 2013; Sardinha et al. 2014; Sani et al. 2015; Scott et al. 2015). Also, microseismic

monitoring can be combined with the pressure test to improve understanding the well interference (Grossi et al. 2015; Lehmann et al. 2016). During the pressure test, all wells are first shut in to build up pressure. After a certain period, some wells are brought back on production in sequence while bottomhole pressure (BHP) or wellhead pressure of the shut-in well is measured (Lindner and Bello 2015). If the well interference occurs through high-conductive connecting fractures, the shut-in well(s) will experience an instantaneous pressure drop. The time might be a few minutes (Awada et al. 2016). **Figure 1** presents an example of interference test for measuring BHP of shut-in Well 5 when opening Wells 1-4 sequentially in Wolfcamp shale, revealing the existence of inter-well connectivity (Scott et al. 2015).

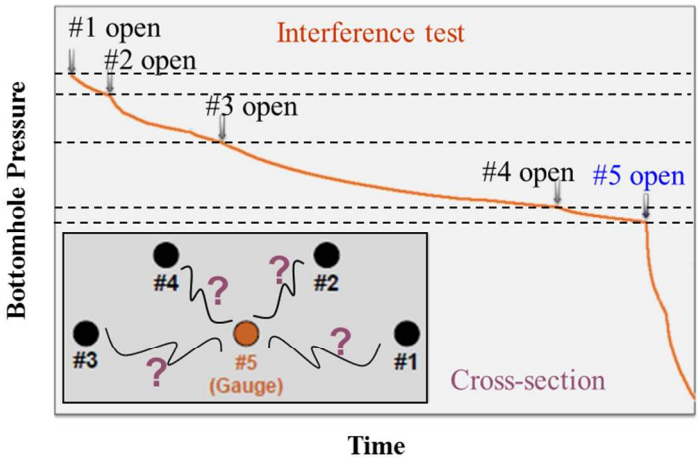

Figure 1. An example of interference test by measuring the bottomhole pressure response of shut-in wells in the Wolfcamp shale. Vertical scale shows BHP in Well 5, which already drops when adjacent wells 1-4 are opened, indicating well interference occurs for all wells (modified from Scott et al. 2015).

Actually, there are many mechanisms to induce well interference, which is a very complex process (King and Valencia 2016). **Figure 2** only presents three possible causes of well interference in a single reservoir layer: (a) interference through matrix permeability; (b) interference through connecting hydraulic fractures; and (c) interference through natural fractures, or a combination of mechanisms (a)-(c). In addition, well interference can occur across different reservoir layers (Lindner and Bello 2015). Any well interference through the matrix in shale formations with ultralow permeability is more limited than that occurring through connecting fractures (Awada et al. 2016). Although numerous pressure tests in the field have proven the existence of well interference (Portis et al. 2013; Sardinha et al. 2014; Sani et al. 2015; Scott et al. 2015), relatively few physical models exist to quantitatively simulate and explain the pressure response of shut-in wells. Marongiu-Porcu et al. (2016) presented a state-of-the-art workflow by combining a complex fracture model, reservoir simulation, and geomechanics model to simulate complex fracture geometry, well performance, and stress properties to minimize undesired fracture hits. Nevertheless, the pressure response of shut-in well(s) was not included in their study.

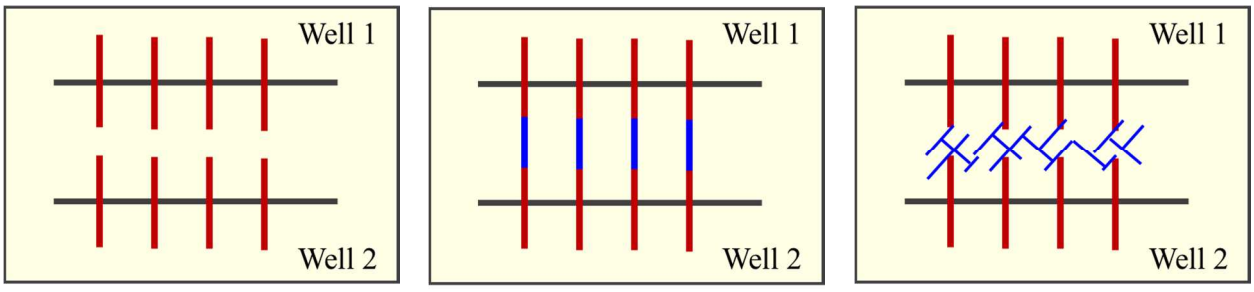

(a) (b) (c)

Figure 2. Three possible mechanisms for inducing well interference (plan view):
(a) through matrix permeability, (b) through connecting hydraulic fractures, (c) through natural fractures.

Recently, Awada et al. (2016) built a simple analytical model to simulate the pressure response of a shut-in well connected to an adjacent vertical well through a single straight fracture hit with uniform fracture conductivity. Constant flow rate of the producer was used as a simulation constraint. The authors examined the effect of hydraulic fracture conductivity on the timing and magnitude of pressure drop of the shut-in well. They found that the fracture conductivity significantly affects the timing and magnitude of well interference. The higher fracture conductivity, the larger the pressure drop of the shut-in well. However, the analytical model is limited for simulating pressure response of multiple horizontal wells, where well-to-well interference occurs through multiple connecting complex fractures. In reality, a complex fracture geometry is often created during the hydraulic fracturing process (Warpinski et al. 2005; Cipolla and Wallace 2014; Sun and Schechter 2015). Also, most fracture propagation models predict the initiation of complex non-planar fracture geometries, especially in the presence of natural fractures (Wu et al. 2012; Xu and Wong 2013; Wu and Olson 2013, 2015). Furthermore, the impact of spatial changes in fracture conductivity, number of connecting fractures, and complex fracture geometry on the pressure response of well interference have not been systematically modeled in prior studies. Although significant efforts have been made to develop semi-analytical models to simulate well performance with complex fracture geometry (Cohen et al. 2012; Zhou et al. 2015; Yu 2015; Yu et al. 2016a), most studies consider only single well and production model of well interference in multiple wells is lacking. Hence, a more-rigorous integrated physical model to simulate the pressure response of well-to-well connectivity with complex fracture geometry is needed.

The purpose of this study is to develop a semi-analytical model to simulate and analyze the pressure change of shut-in well(s) for complex well interference systems. We verify the model against a numerical reservoir simulator for simulation of well performance and pressure change in a two-well system with and without connecting fracture(s). After verification, we examine the effects of connecting fracture conductivity, hydraulic fracture conductivity, and matrix permeability on pressure response in two fractured vertical wells. In addition, we investigate the effect of number of connecting fractures on well interference in two fractured horizontal wells. Furthermore, we apply a complex fracture propagation model to investigate the influence of complex connecting fractures on well interference with and without the presence of natural fractures. We also apply an analytical streamline model developed to visualize the stimulated rock volume. Our study provides an improved fundamental understanding of the influence of key reservoir and fracture properties on well interference.

Semi-Analytical Model Development

In order to simulate well performance of multiple wells with complex non-planar fracture geometry, the semi-analytical model will discretize the complex fractures into a number of small fracture segments with the associated nodes. **Figure 3** presents an example of discretized fractures in two horizontal wells with eight non-planar hydraulic fractures and four fracture hits. The ideal number of discretized segments is mainly dependent on the complexity of the fracture geometry. In the example of Figure 3, the total number of fracture segments is determined as 51 (numbering in red color sequentially) and the corresponding number of nodes is 55 (numbering in black color sequentially). Each fracture segment has specific properties such as fracture length, fracture orientation, and fracture aperture. The model thus approximately represents non-planar fractures with non-uniform spatial distribution of fracture conductivity. Production of unconventional oil and gas from shale formation mainly consists of two parts: fluid flow from shale matrix into fracture and fluid flow from fracture to wellbore. In the following sections, we will introduce the corresponding fundamental flow equations.

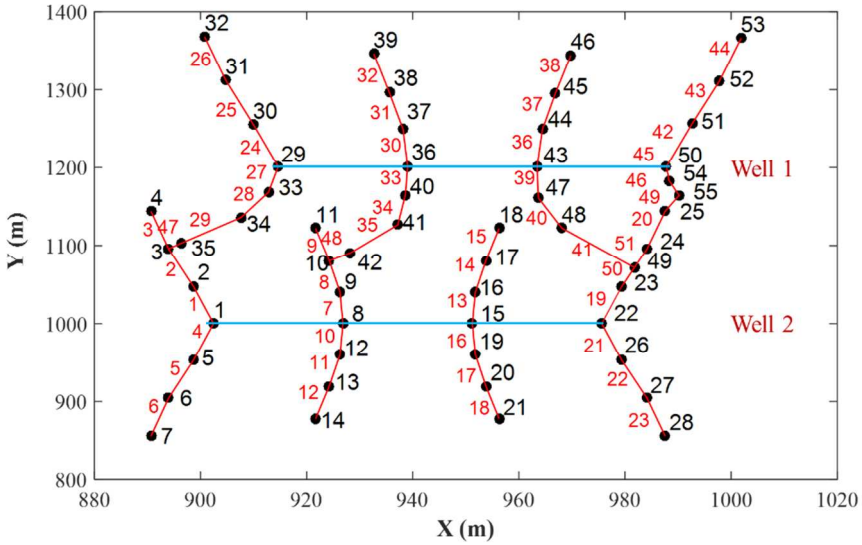

Figure 3. Plan view of a reservoir slab with two horizontal wells in a fracture section of eight non-planar fractures interconnected across the two wells. Fractures are discretized into segments in order to capture the complex non-planar fracture geometry.

Fluid flow from shale matrix into fracture. In this study, we focus on the simulation of oil production from tight formations. Hence, we make several key assumptions for the semi-analytical model:

- The reservoir is bounded by an upper and a lower impermeable layer;
- The reservoir is isotropic and homogeneous;
- The reservoir is an infinite slab with constant reservoir thickness;
- Fluid has constant density, viscosity, and compressibility;
- Fractures fully penetrate reservoir thickness;
- Initial reservoir pressure is uniform;
- There is no pressure loss along wellbores;
- There is no gravity effect.

Under these assumptions, the following two-dimensional (2D) unsteady-state diffusivity equation can be utilized to model oil flow from the matrix into a fracture system (Thambynayagam 2011):

$$\eta_x \frac{\partial^2 p}{\partial x^2} + \eta_y \frac{\partial^2 p}{\partial y^2} = \frac{\partial p}{\partial t}, \tag{1}$$

where p is pressure, η_j ($j = x, y$) is the hydraulic diffusivity coefficient and defined as:

$$\eta_j = \frac{k_j}{\phi c_t \mu}, \tag{2}$$

where k_j is permeability along the *j*-th coordinate, ϕ is porosity, c_t is total compressibility, and μ is oil viscosity.

The Green's functions and source solutions are often used to solve this unsteady-state diffusivity equation (Gringarten et al. 1972; Gringarten and Rameny 1973). In this study, each fracture segment can be treated as a plane sink. **Figure 4** shows the *j*-th segment with an inclination angle of θ_j ($0^o \le \theta_j < 180^o$) and two nodes j and $j+1$. In addition, each fracture segment is assumed to have uniform flux distribution. A 2D analytical solution below can be utilized to calculate pressure $p(x, y, t)$ at any location with respect time when simulating oil flow from matrix into single fracture segment (Gringarten and Rameny 1973; Guppy et al. 1982):

$$p(x,y,t)=p_i-\frac{U(t-t_0)}{4\pi h_f c_t \rho\phi\eta}\int_0^{t-t_0}\int_{-dl_j/2}^{dl_j/2}\frac{q_{fj}(\tau)}{t-t_0-\tau}\times e^{-\frac{\left(x+x'\cos\theta_j-\frac{x_j+x_{j+1}}{2}\right)^2+\left(y+x'\sin\theta_j-\frac{y_j+y_{j+1}}{2}\right)^2}{4\eta(t-t_0-\tau)}}\mathrm{d}x'\mathrm{d}\tau, \quad (3)$$

where p_i is initial reservoir pressure, $U(t-t_0)=\begin{cases}0, & t<t_0\\ 1, & t>t_0\end{cases}$ is the Heaviside's unit step function, q_{fj} is the flux of the *j*-th fracture segment, h_f is fracture height, ρ is oil density, η is the hydraulic diffusivity coefficient ($\eta=\eta_x=\eta_y$), dl_j is the length of the *j*-th fracture segment. Considering interference between multiple wells and multiple fracture segments, the superposition principle can be used to calculate the pressure by adding the contributions from all fracture segments:

$$p(x,y,t)=p_i-\frac{U(t-t_0)}{4\pi h_f c_t \rho\phi\eta}\sum_{j=1}^{N_f'}\int_0^{t-t_0}\int_{-dl_j/2}^{dl_j/2}\frac{q_{fj}(\tau)}{t-t_0-\tau}\times e^{-\frac{\left(x+x'\cos\theta_j-\frac{x_j+x_{j+1}}{2}\right)^2+\left(y+x'\sin\theta_j-\frac{y_j+y_{j+1}}{2}\right)^2}{4\eta(t-t_0-\tau)}}\mathrm{d}x'\mathrm{d}\tau, \quad (4)$$

$$N_f'=\sum_{i=1}^{N_w}N_{fi}, \quad (5)$$

where N_w is number of well, N_{fi} is number of fracture segment in the *i*-th well.

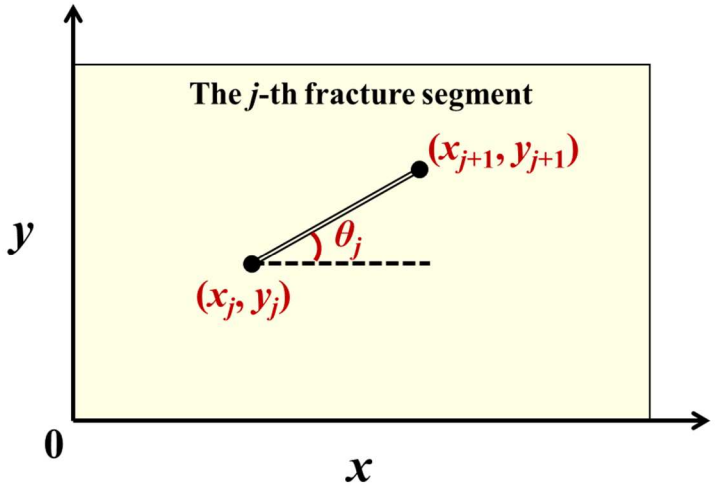

Figure 4. One fracture segment with an inclination angle of θ_j that links the node *j* and the node *j*+1.

Fluid flow from fracture to wellbore. Zhou et al. (2013) provided an expression for describing fluid flow along each fracture segment by considering the non-Darcy effect. As shown in Figure 4, assuming the pressure (p_j) at the node j is larger than the pressure (p_{j+1}) at the node $j+1$, the equation for modeling fluid flow in the fracture is given by

$$p_j-p_{j+1}=\int_{y_j}^{y_{j+1}}D_j q_j(y)+ND_j q_j(y)^2\,dy, \quad (6)$$

where $q_j(y)=q_j+q_{fj}(y-y_j)/\sin\theta_j$, q_j is fluid flow rate at the node j of the *j*-th fracture segment, the coefficient of Darcy flow is $D_j=\mu/\rho h_f(k_f w_f)_j$, k_f is fracture permeability, w_f is fracture width, the

coefficient of non-Darcy flow is $ND_j = \rho\beta \Big/ \left(\rho w_f h_f\right)_j^2$, β is the non-Darcy Forchheimer coefficient. In this study, we assume the oil flow in the fracture obeys Darcy's law.

Model Unknowns, Governing Equations, and Model Solution

A constant BHP is used as a simulation constraint of the semi-analytical model. For the multiple-well system each well can be given a different BHP value. It should be noted that the model can be easily extended to handle the simulation with constant flow rate constraint. By considering the total number of fracture segments (N_f') and the associated total number of nodes (N_v'), the unknowns that need to be solved for the multiple well model are:

- N_f' oil flux at the fracture segments of all wells, q_{fj}, $j = 1, \ ..., N_f'$.
- N_v' oil flow rates at the nodes of all wells, q_j, $j = 1, \ ..., N_v'$.
- N_v' pressure at the nodes of all wells, p_j, $j = 1, \ ..., N_v'$.

Hence, the total number of unknowns is $N_f' + 2N_v'$. In order to solve the unknowns we need to apply a corresponding number of independent, governing equations as follows:

- N_f' pressure equations for the fracture segments of all wells using Eq. (6); in addition, there are $N_v' - N_f'$ known BHP from multiple wellbores, where each well can have different values.
- N_f' pressure continuity equations for each fracture segment by equating Eq. (4) to Eq. (6). The fracture center at each segment is selected in this study and the expression is given below by considering Darcy flow:

$$p_i - \frac{U\left(t-t_0\right)}{4\pi h_f c_t \rho\phi\eta} \sum_{j=1}^{N_f'} \int_0^{t-t_0} \int_{-dl_j/2}^{dl_j/2} \frac{q_{fj}\left(\tau\right)}{t-t_0-\tau} \times e^{-\frac{\left(x'\cos\theta_j\right)^2 + \left(x'\sin\theta_j\right)^2}{4\eta(t-t_0-\tau)}} \mathrm{d}x'\mathrm{d}\tau$$
$$= p_j - \int_{y_j}^{y_{jc}} \left(\mu / \rho h_f k_f w_f\right)_j \left[q_j + q_{fj}\left(y - y_j\right)/\sin\theta_j\right] dy \quad , \quad j = 1, \ ..., N_f', \tag{7}$$

where y_{jc} is the y coordinate of center point of the *j*-th fracture segment.

- N_v' mass balance equations at the nodes of all wells:

$$q_j = \sum_{k=1}^{N_{cn}} \left(q_k + q_{fk} dl_k\right), \ j = 1, \ ..., N_v', \tag{8}$$

where N_{cn} is the number of connecting nodes with the *j*-th node. Note that for the end notes, we assume that there is no fluid entering.

Figure 5 presents the flowchart for the semi-analytical model to simulate well performance and pressure of multiple wells. The semi-analytical model was solved using a computer program. It is important to point out that the semi-analytical model can use varying time steps, which can significantly improve the computational efficiency. In general, a small time step is considered for the early time simulations, while a large time step is recommend for the late time simulations.

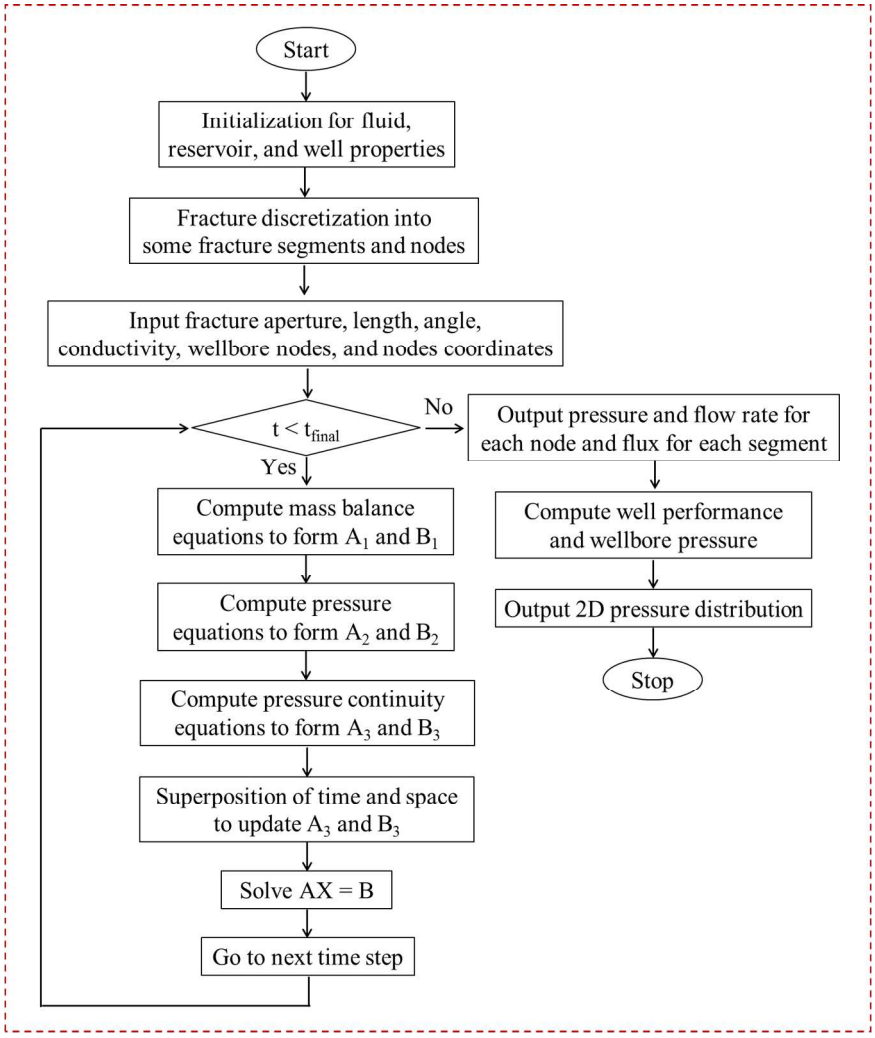

Figure 5. Flowchart for the semi-analytical model to simulate well performance and pressure of multiple wells.

Analytical Model for Streamline Visualization

In addition to the numerical and semi-analytical modelling tools, an analytical method was used for the visualization of streamlines, progressive drainage and quantification of the time-of-flight. The model takes inputs from the semi-analytical models to correctly scale the flux strength from the matrix into each fracture segment as it drains the reservoir. A reservoir simulator (numerical and semi-analytical) can attribute the overall pressure declines and flux rate contributions to individual fracture segments using either real or synthetic reservoir data. The flux rates generated by the reservoir simulator capture all the relevant reservoir physics and can be fed into the parallel analytical streamline simulator (PASS; Weijermars et al. 2016). PASS allows flow modelling near any fracture network and uses line-source/sink elements strung together to represent the fracture network.

Our method for visualizing the progressive drainage of the SRV (stimulated reservoir volume) near the fracture stages is based on complex analysis. The analytical particle path solutions have been benchmarked and validated using independent ECLIPSE-based streamline solutions (Weijermars et al. 2016). In complex analysis, the velocity field $V(z)$ for a general interval-source located on the interval $[z_a, z_b]$ between $z_a(=a+i\cdot c)$ and $z_b(=b+i\cdot d)$ is:

$$V(z)=\frac{m^*(t^*)}{z_b-z_a}\left[\log(z-z_a)-\log(z-z_b)\right]. \tag{9}$$

By Eq. (9), we can obtain the velocity distribution over all the reservoir and calculate the streamline trajectories and time of fight contour. More details about the analytical method application in our study are given in Appendix A1.

In **Figure 6**, the flowchart for the analytical method is illustrated. The semi-analytical fracture flux model provides inputs for the analytical drainage simulator typically in dimensional units whereas the analytical simulator typically uses non-dimensional units. Dimensional analysis can be applied to relate the dimensional quantities of the prototype reservoir to the non-dimensional quantities of the analytical drainage visualization model (Weijermars and Schmeling 1986; Weijermars et al. 2016). Alternatively, dimensional units are used directly in the analytical model which was preferred in our present study. The dimensional $Q(t)$ is the flux rate in bbl/day provided by the reservoir simulator relates to the dimensional line source strength $m(t)$ as follows:

$$m(t) = \frac{5.6145 Q(t)}{2\pi\phi h}, \tag{10}$$

where ϕ is reservoir porosity and h is the reservoir thickness. Derivation details and additional examples of scaling are given in Appendix A2.

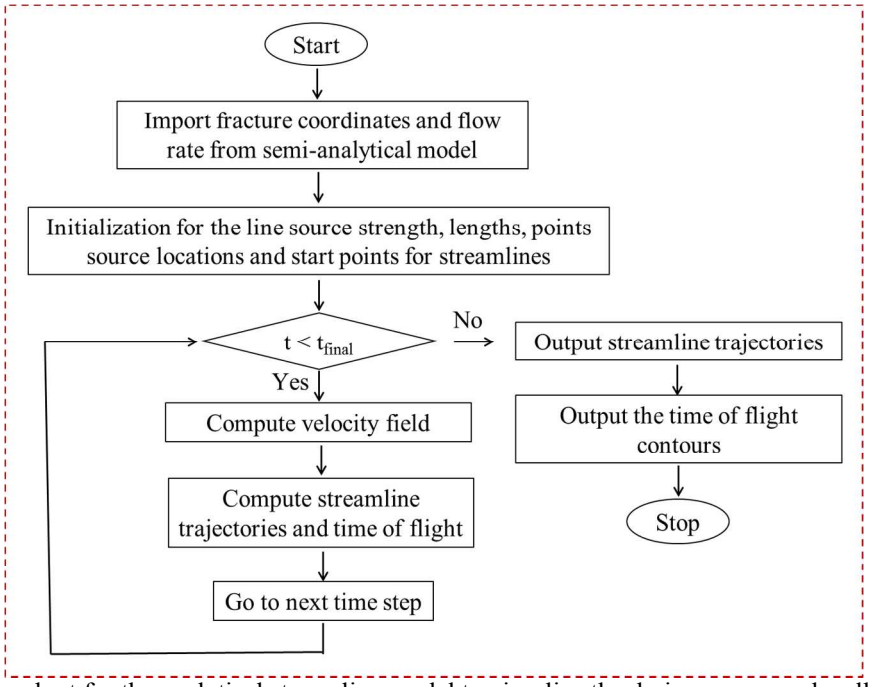

Figure 6. Flowchart for the analytical streamline model to visualize the drainage area and well interference.

Model Verification

We verified the semi-analytical model against a numerical reservoir simulator (CMG-IMEX 2012) for two horizontal wells with and without considering well interference through fracture hits, as shown in **Figure 7**. The distance of two wells is 660 ft. Each well has four simple planar hydraulic fractures with equally fracture spacing. The local grid refinement (LGR) approach is used to explicitly model hydraulic fractures for the numerical model (Yu et al. 2016b). The basic reservoir and fracture properties used for simulations are summarized in **Table 1**. The BHP is held at 3,000 psi for each well. Fracture conductivity of all hydraulic and connecting fractures is assumed to be 100 md-ft. The simulation time is 1,000 days.

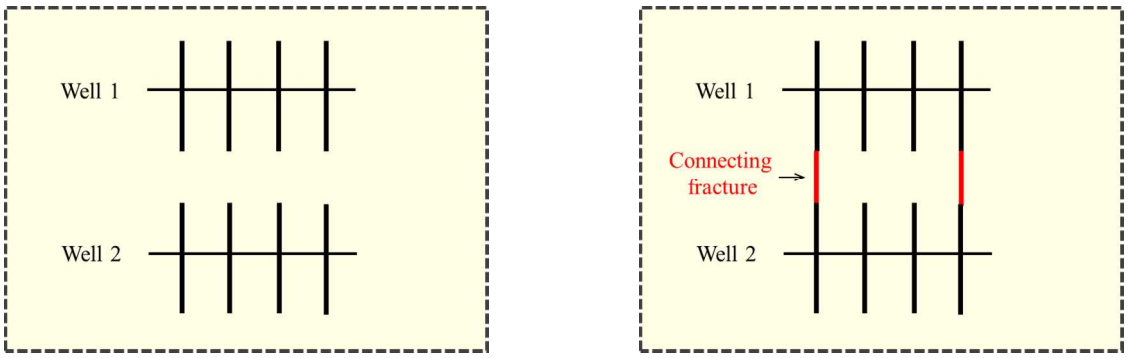

(a) (b)

Figure 7. Verification of semi-analytical model against numerical model for two horizontal wells with and without considering well interference through fracture hits. (a) No fracture hits (b) Two fracture hits (in red color).

Table 1: Basic reservoir and fracture properties used for verification

Parameter	Value	Unit
Initial reservoir pressure	8,000	psi
Reservoir temperature	240	^{o}F
Reservoir thickness	50	ft
Reservoir permeability	0.01	mD
Reservoir porosity	7%	-
Oil viscosity	0.6	cp
Formation volume factor	1.273	bbl/STB
Fracture spacing	80	ft
Total compressibility	1×10^{-6}	psi^{-1}
Fracture half-length	210	ft
Fracture conductivity	100	md-ft
Fracture height	50	ft
Fracture width	0.01	ft

Figure 8 shows the comparison of oil flow rate obtained from the semi-analytical model and the numerical model. It can be seen that a good match is obtained for each scenario. Accordingly, the semi-analytical model can accurately simulate tight oil production from multiple horizontal wells with and without considering the well interference through connecting fractures. Additionally, the pressure distribution for each scenario after 30 days of production is visualized in **Figure 9**. The solid lines in the figure represent the fracture geometry. The pressure distribution around the fractures is different for the two cases compared in Figures 9(a) and 9(b).

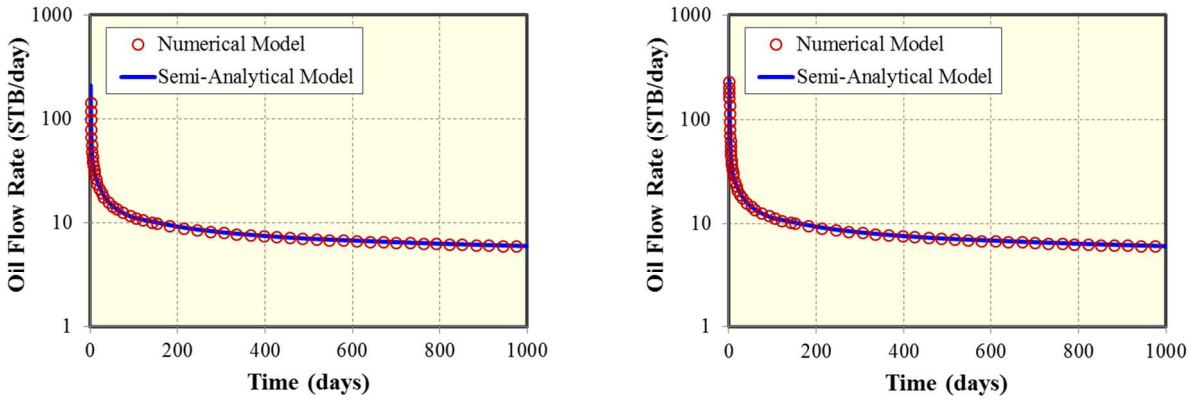

(a) (b)

Figure 8. Comparison of oil flow rate from the semi-analytical model and the numerical model.
(a) No well interference through fracture hits (b) Well interference through fracture hits

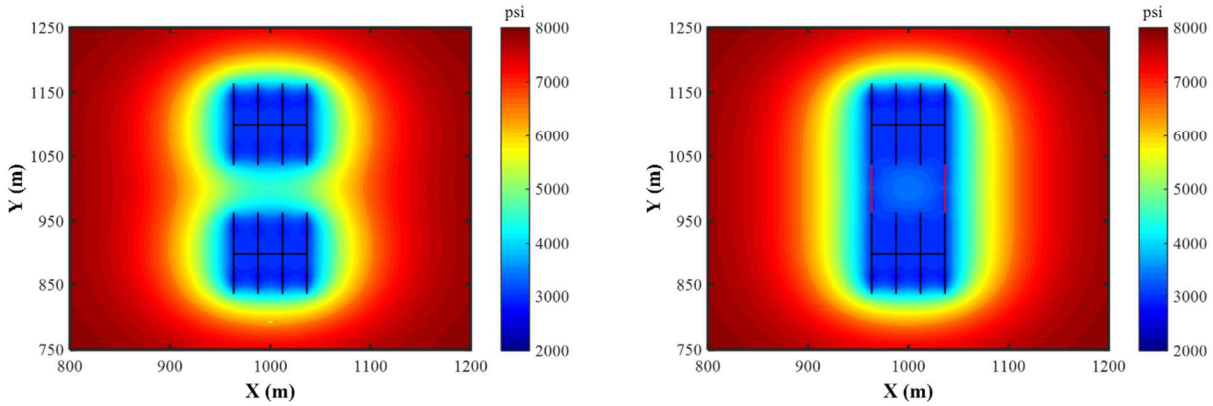

Figure 9. Comparisons of pressure distribution after 30 days of production for two scenarios. (a) No well interference through fracture hits (b) Well interference through fracture hits

Furthermore, we verified the semi-analytical model against the numerical model for two vertical fractured wells, as shown in **Figure 10**. There is a single straight fracture hit between two wells. Well 1 is shut in and Well 2 is producing under the constraint of BHP of 3,000 psi. The other reservoir and fracture properties remain the same as Table 1. The comparison of BHP of shut-in Well 1 between the semi-analytical model and the numerical model is displayed in **Figure 11**, illustrating that a good match between them is obtained. Hence, the semi-analytical model has the capability of accurately simulating the pressure response of the shut-in well when the occurrence of well interference due to the fracture hit.

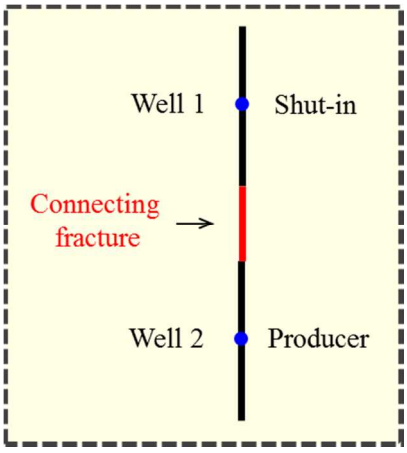

Figure 10. Plan view of two vertical wells each with a bi-wing fracture with interference through a single straight fracture hit.

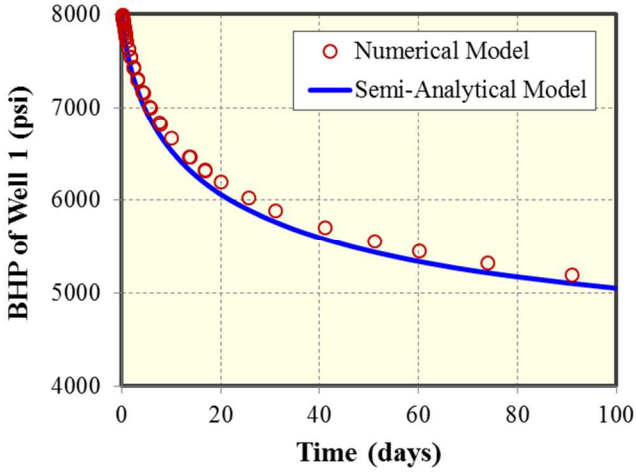

Figure 11. Comparison of the BHP of Well 1 according to the semi-analytical model and the numerical model.

Simulation Studies

After model verification, we performed a series of case studies to investigate the pressure response of the shut-in well when well interference occurs due to the fracture hits. The slanted and complex geometries of connecting fracture(s) are also taken into account. We evaluated three scenarios of fracture hits for two wells: a single slanted fracture hit, multiple slanted fracture hits, and multiple complex fracture hits.

For the last scenario, a complex hydraulic fracture propagation model, developed by Wu and Olson (2015a, 2016) was applied to generate the non-planar fracture geometry around the two wells with and without considering the natural fractures. The fracture propagation model couples rock deformation and fluid flow in the fractures and

horizontal wellbore. Fracture opening and shearing are determined using a simplified three-dimensional displacement discontinuity as proposed by Wu and Olson (2015b). Fluid flow in the fracture and the associated pressure drop are based on lubrication theory, assuming the fracture is analogous to a slot between parallel plates and the fluid is non-Newtonian with a power-law behavior. The total fluid injected into the horizontal wellbore is assumed to be constant. Partitioning of flow rate into each fracture is dynamically calculated in such way that the wellbore pressure is constrained to gradually decrease along the lateral due to wellbore friction. The interaction of hydraulic and natural fractures is described through analyzing induced stresses at the fracture tips. A stochastic realization method are used to generate natural fracture patterns. Additionally, it is assumed that length of natural fractures follows a power-law distribution. In this study, we assumed that all natural fractures were sealed. Without interacting with hydraulic fractures, natural fractures did not contribute to production. Physical mechanisms of complex fracture geometry are handled by the numerical model through incorporating the stress shadow effects, flow rate distribution among multiple fractures, and interaction of hydraulic and natural fractures. The model has been validated against known analytical solutions for single hydraulic fracture growth (Olson and Wu 2012). To demonstrate the validity of capturing the physical process of fracture interaction, the model has also been compared to a numerical model (Wu et al. 2012) in case of multiple fracture propagation.

Single slanted fracture hit. Figure 12 is the configuration of two vertical fractured wells, where two hydraulic fractures are placed in a staggered manner. The horizontal distance between the two fractures is 40 ft. There is a single slanted fracture hit to connect two hydraulic fractures. Note that it is difficult to simulate this situation using a traditional numerical reservoir simulator with structured grids. The distance of two wells is 660 ft. The other reservoir and fracture properties remain the same as Table 1. We first examined the role of connecting fracture conductivity in pressure response of shut-in Well 1, as shown in **Figure 13**. The connecting fracture conductivity ranges from 0.1 to 100 md-ft. Two hydraulic fracture conductivities are held constant at 100 md-ft. Our experiments show that an increase in connecting fracture conductivity leads to a decrease of BHP in Well 1 at corresponding times [Figure 13(b)]. For the value of connecting fracture conductivity of 100 md-ft, the BHP of Well 1 decreases much faster than the other values at a short-term period of production. As shown in Figure 13(b), the well interference happens immediately after Well 2 begins producing for the conductivities of 10 and 100 md-ft. It can be suggested that fluid pressure transfer from shut-in Well 1 to producing Well 2 is easier when the connecting fracture conductivity is larger. The pressure decline for conductivities of 0.1, 1, 10, and 100 md-ft after 30 years is not converging [Figure 13(a)]. In general, the period of practical well-interference test is short. Hence, most of our pressure response simulation studies are limited to 100 days.

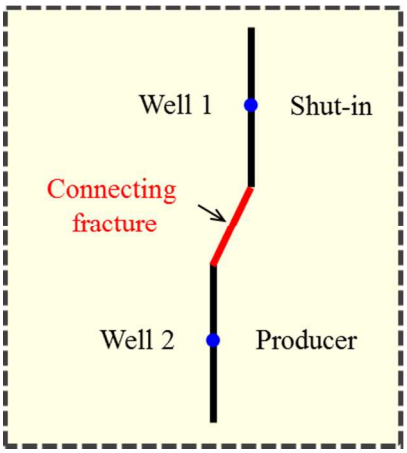

Figure 12. Well interference for two vertical fractured wells through single slanted fracture hit.

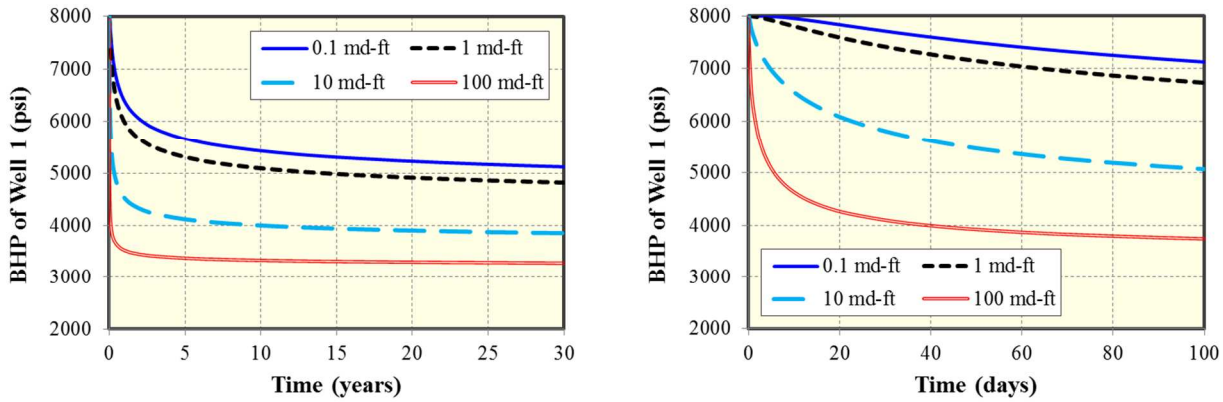

(a) (b)

Figure 13. Effect of the connecting fracture conductivity on BHP of Well 1.
(a) For a long-term period of 30 years (b) For a short-term period of 100 days

We also performed sensitivity studies for the impacts of matrix permeability and primary hydraulic fracture conductivity on pressure response of shut-in Well 1. **Figure 14** uses matrix permeability ranging from 0.001 to 0.1 md, the connecting fracture conductivity is 10 md-ft and hydraulic fracture conductivities are 100 md-ft. The other properties remain the same as in Table 1. As shown in Figure 14(a), the higher the permeability is, the smaller the drop in BHP will be. This means that the well interference phenomenon will become more severe for tighter reservoirs with ultralow matrix permeability. For the effect of primary hydraulic fracture conductivity, range of 1-100 md-ft is considered, the connecting fracture conductivity is held at 1 md-ft and matrix permeability is 0.01 md. As shown in Figure 14(b), with increasing hydraulic fracture conductivity, the pressure drop of Well 1 increases, indicating that the well interference is more severe. **Figure 15** presents the pressure distribution after 30 days for the situation of connecting fracture conductivity of 10 md-ft, hydraulic fracture conductivity of 100 md-ft, and matrix permeability of 0.01 md. As shown, the shut-in Well 1 is drained with Well 2 depletion due to the well interference through single slanted fracture hit. **Figure 16** visualizes the progressive advancement of reservoir drainage area and well interference around the two interconnected fractures across each well. Streamlines are highlighted blue and the red lines are time of flight contours spaced for 30 days. Total drainage area shown is for 300 days of production with a single slanted fracture hit. Two additional case studies with extreme lower and upper bounds for fracture conductivity and matrix permeability were investigated and are presented in Appendix B.

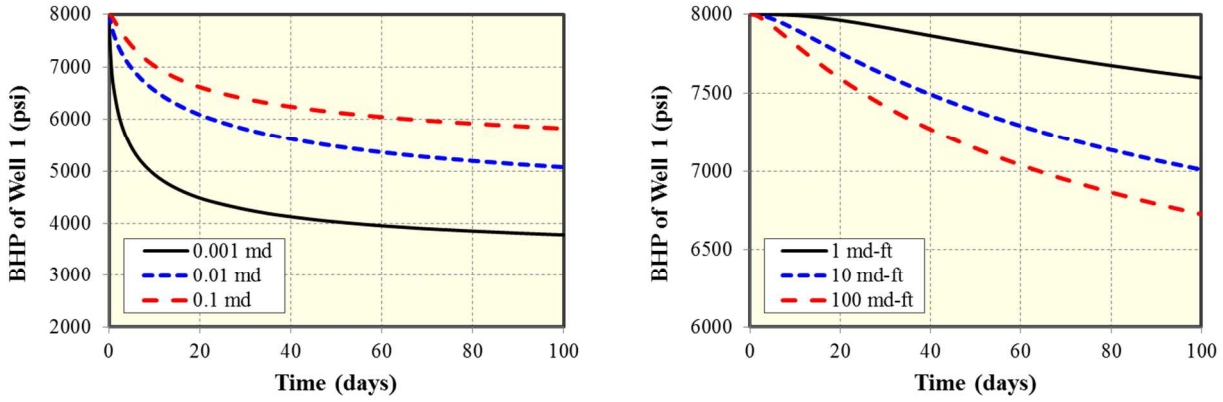

(a) (b)

Figure 14. Effects of matrix permeability and hydraulic fracture conductivity on BHP of Well 1.
(a) Effect of matrix permeability (b) Effect of hydraulic fracture conductivity

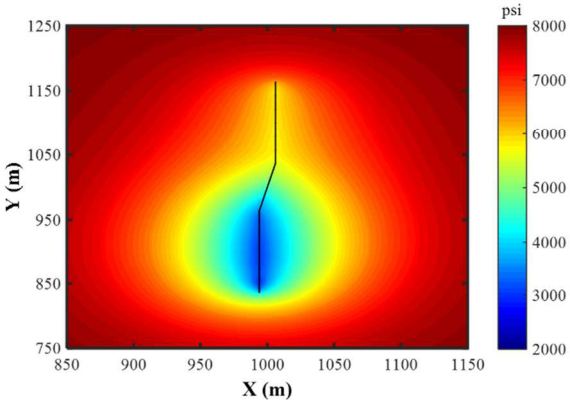

Figure 15. Pressure distribution after 30 days of production for single slanted fracture hit.

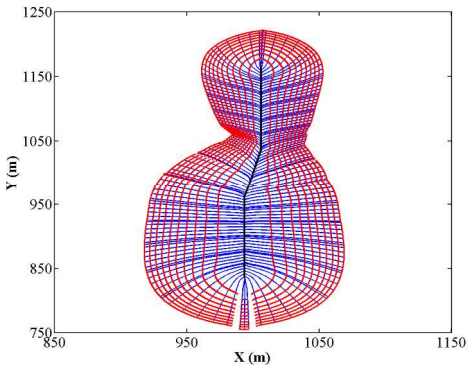

Figure 16. Streamlines trajectories in blue and time of flight contours in red for the geometry in Figure 15.

Multiple slanted fracture hits. Figure 17 presents the configuration of two horizontal wells with two slanted fracture hits for inducing well interference. It should be noted that four wellbore nodes of shut-in Well 1 are connected through a highly conductive fracture with large conductivity of 10,000 md-ft in this study, while there is no adjacent matrix flux. This approach can approximately and effectively maintain a smooth pressure response in an actual wellbore and avoid a severe pressure fluctuation along the wellbore. The connecting slanted fracture conductivity is 10 md-ft, hydraulic fracture conductivities are 100 md-ft, and matrix permeability is 0.01 md. The other properties remain the same as Table 1. The BHP of Well 1 for four wellbore nodes is shown in **Figure 18**, which indicates that the pressure profile along the wellbore is smooth and equal at all times while the reservoir progressively depletes.

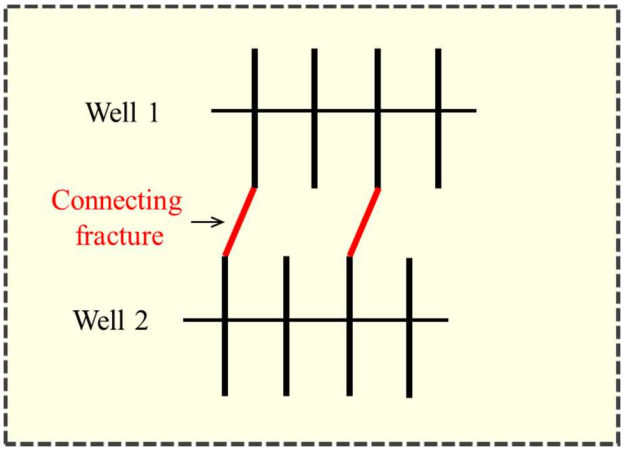

Figure 17. Well interference for two horizontal wells through two slanted fracture hits.

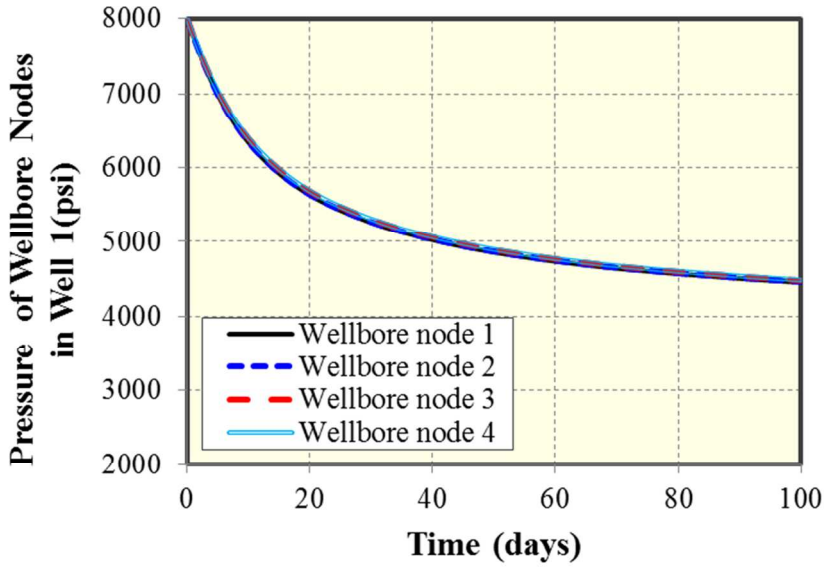

Figure 18. Comparison of pressure response of four wellbore nodes in Well 1.

In addition to the two fracture hits, we examined various numbers of slanted fracture hits: 1, 3, and 4, as shown in **Figure 19**. **Figure 20** presents the impact of the number of fracture hits on the BHP of Well 1. As shown, the pressure decline of Well 1 is faster when the number of fracture hits increases. This means that all other properties being equal, the well interference will adversely affect production of Well 1 when the number of fracture hits increases. Hence, it is very important to better characterize the number of connecting fractures in conjunction with the real interference test data. **Figure 21** visualizes the comparison of pressure distribution after 30 days between 2 fracture hits and 4 fracture hits, clearly indicating that the pressure drop of Well 1 with 4 fracture hits is larger than that with 2 fracture hits.

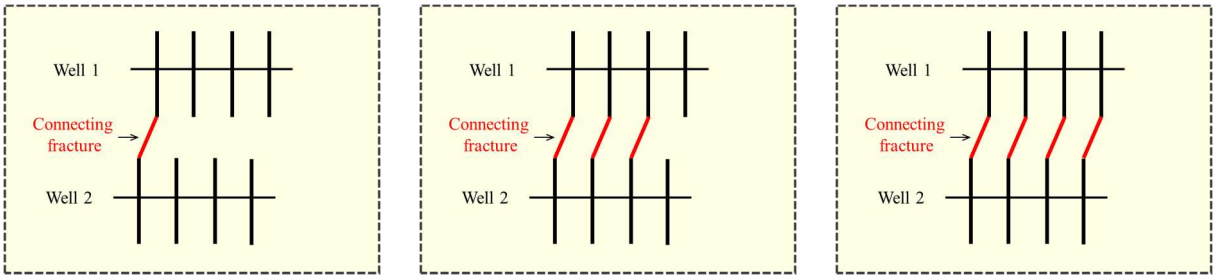

(a) (b) (c)

Figure 19. Schematic of different number of fracture hits on well interference for two horizontal wells.
(a) Single slanted fracture hit (b) Three slanted fracture hits (c) Four slanted fracture hits

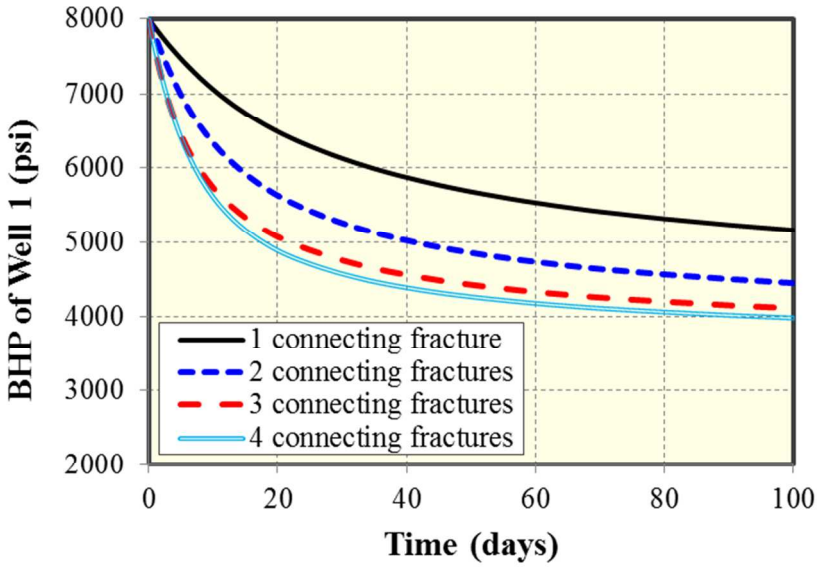

Figure 20. Effect of number of connecting fracture on BHP of Well 1.

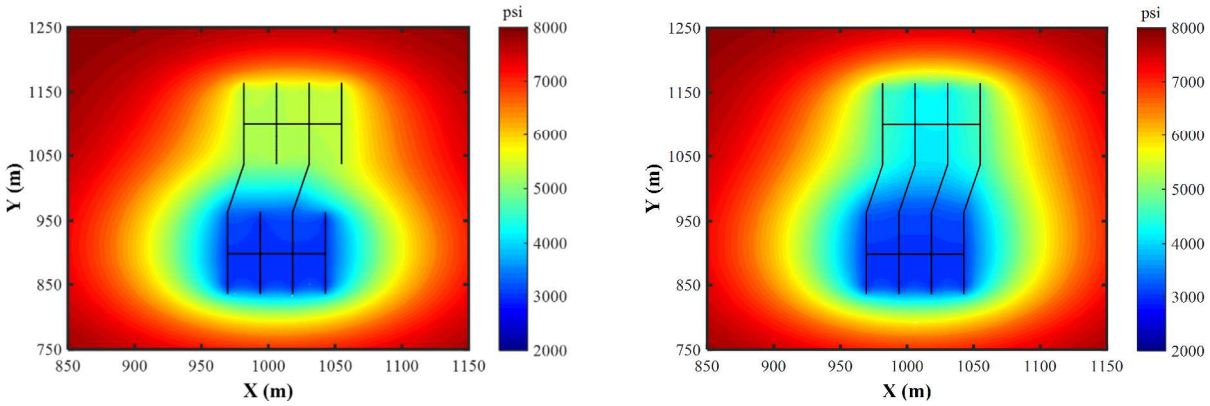

(a) (b)

Figure 21. Comparison of pressure distribution after 30 days for well interference with two and four fracture hits.
(a) Two slanted fracture hits (b) Four slanted fracture hits

Multiple complex fracture hits. Figure 22 presents the configuration of fracture width distribution in two horizontal wells with multiple complex fracture hits with and without natural fractures, which were generated based on the complex fracture propagation model. As shown, the fracture geometry is more complex at the presence of the natural fractures. The injection rate is 60 bpm for each well. Poisson ratio is 0.2. Young's modulus is 4×10^6 psi. The maximum horizontal stress is 4,550 psi and the minimum horizontal stress is 4,450 psi. The leak-off coefficient is 5×10^{-4} ft/min$^{0.5}$. Two sets of natural fractures have orientation of 45^o and 135^o from *x*-axis, respectively. The other reservoir properties remain the same as in Table 1. **Figure 23** compares the BHP of Well 1 for two cases, indicating that the pressure drop without natural fractures is larger than that with natural fractures. Fracture width gradually decreases from wellbore to fracture tips without perturbation of natural fractures. However, when a hydraulic fracture encounters a natural fracture and propagates along it, the fracture width on the natural fracture segment will be restricted. As shown in Figure 22(b), the colors indicated fracture width distribution from wellbore to tips do not gradually change from red to blue. This width restriction acts as a choke to alleviate well interference (Figure 23). Hence, the complex non-planar fractures in Figure 22(a) make fluid transport from Well 1 to Well 2 much easier than that in Figure 22(b). **Figure 24** demonstrates the comparison of pressure distribution after 30 days of production, clearly indicating that the difference of intensity of well interference between two cases.

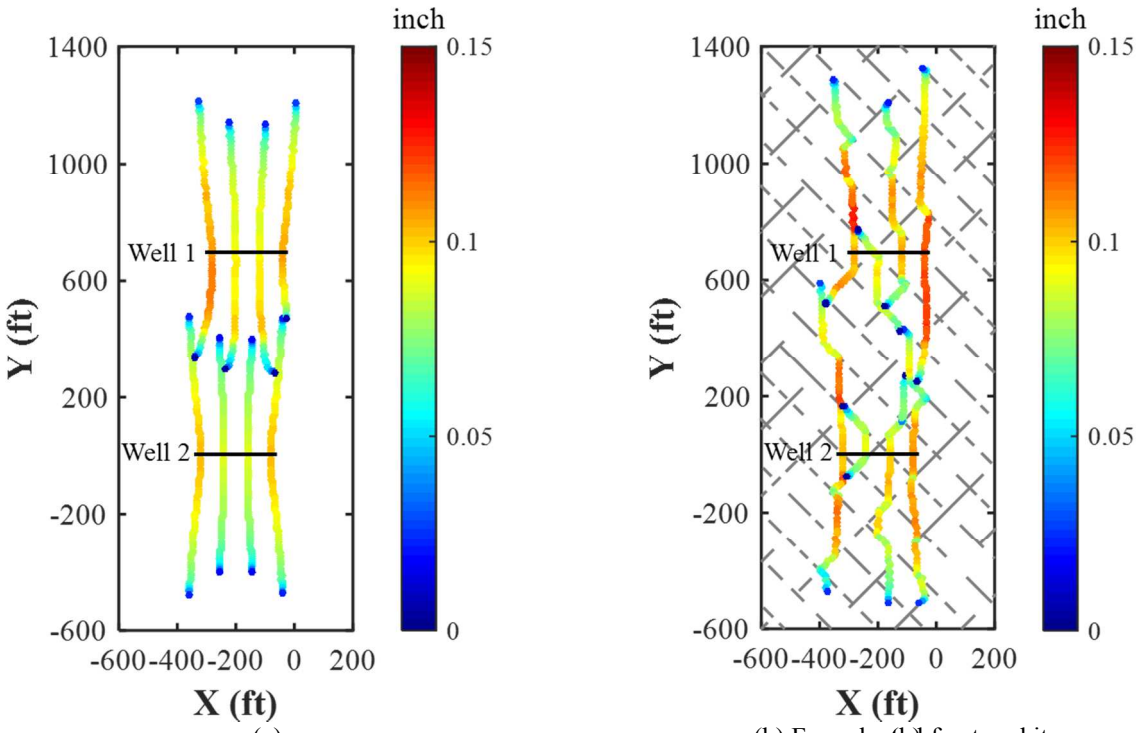

Figure 22. Fracture width distribution in two horizontal wells with well interference through multiple complex fracture hits.
(a) Two slanted fracture hits (b) Four slanted fracture hits

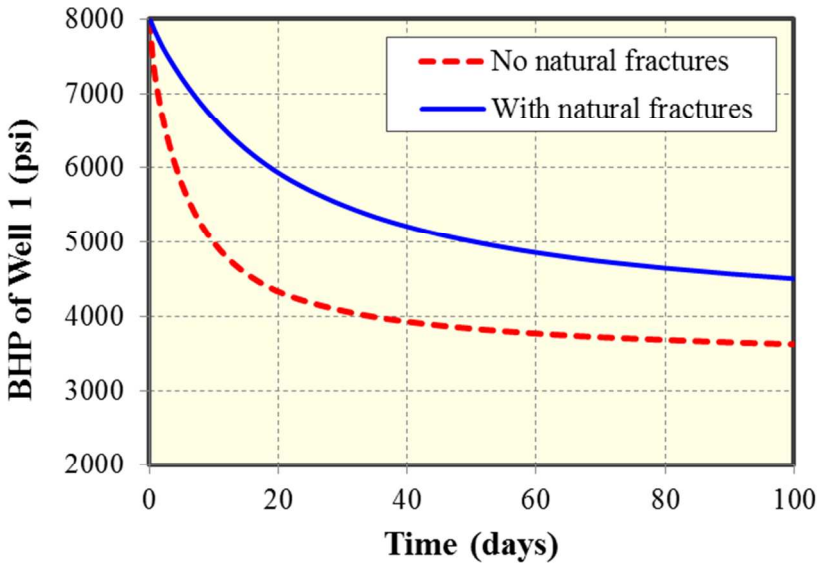

Figure 23. Comparison of BHP of Well 1 between two cases with and without natural fractures.

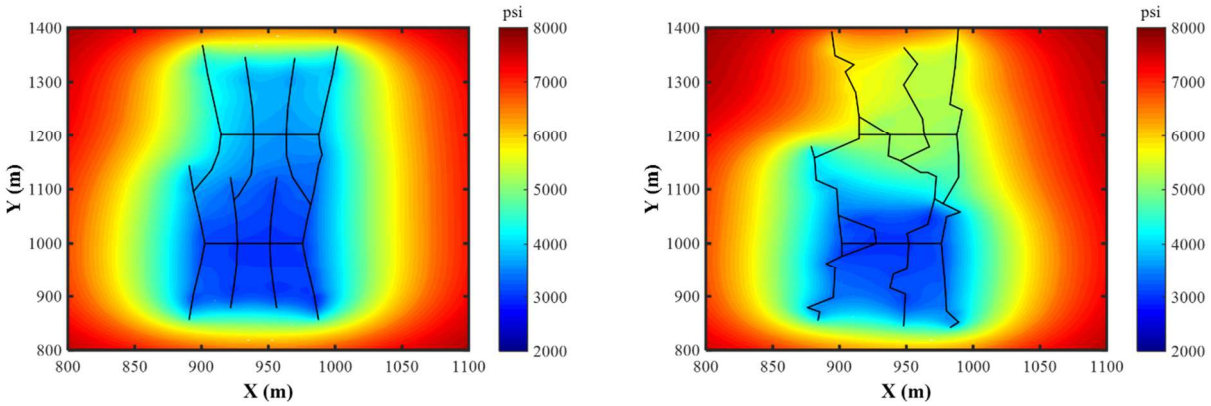

(a) (b)

Figure 24. Comparison of pressure distribution after 30 days for well interference with and without natural fractures.
(a) Without natural fracture effect (b) With natural fracture effect

Conclusions

We proposed a semi-analytical model to simulate well performance and pressure response of well interference through fracture hits. We verified the model against a numerical model. Three scenarios of well interference were examined: (1) a single slanted fracture hit, (2) multiple slanted fracture hits, and (3) multiple complex fracture hits. For all cases we investigated the impacts of fracture conductivity, matrix permeability, number of connecting fracture, and natural fractures on the pressure response. The following conclusions can be drawn from this study:

(1) A good match of well performance in the semi-analytical model and numerical reservoir simulator is obtained for two horizontal wells with and without fracture hits.
(2) A good match of pressure response of shut-in well occurs in the model and numerical reservoir simulator for two vertical wells connected through a single straight fracture hit.
(3) For well interference by a single slanted fracture hit in two vertical fractured wells, the pressure drop of the shut-in well increases when the connecting fracture conductivity and primary fracture conductivity increases. A decrease in pressure drop occurs when the matrix permeability increases.
(4) The drainage area was visualized and time of light was quantified using an analytical streamline model to visualize the effects of well interference.
(5) For well interference through multiple slanted fracture hits in two horizontal fractured wells, the pressure decline of the shut-in well increases when the number of connecting fractures increases.
(6) For well interference through multiple complex fracture hits in two horizontal fractured wells, the pressure decline of the shut-in well is larger without the natural fracture effect than that with the natural fracture effect.

Acknowledgements

The authors would like to acknowledge financial supports from Texas A&M Engineering Experiment Station (TEES). We would also like to acknowledge Computer Modeling Group Ltd. for providing the CMG-IMEX software for this study.

Nomenclature

BHP	=	Bottomhole pressure
CMG	=	Computer Modeling Group
LGR	=	Local grid refinement
SRV	=	Stimulated reservoir volume
p	=	Pressure
η_j	=	Hydraulic diffusivity coefficient ($j = x, y$)

k_j = Permeability along the *j*-th coordinate

ϕ = Porosity

c_t = Total compressibility

μ = Oil viscosity

θ_j = An inclination angle of the *j*-th segment ($0^o \le \theta_j < 180^o$)

p_i = Initial reservoir pressure

q_{fj} = Flux of the *j*-th fracture segment

h_f = Fracture height

ρ = Oil density

dl_j = Length of the *j*-th fracture segment

N_w = Number of well

N_{fi} = Number of fracture segment in the *i*-th well

q_j = Fluid flow rate at the node *j* of the *j*-th fracture segment

D_j = Coefficient of Darcy flow of the *j*-th fracture segment

ND_j = Coefficient of non-Darcy flow of the *j*-th fracture segment

k_f = Fracture permeability

w_f = Fracture width

β = Non-Darcy Forchheimer coefficient

N_f' = Total number of fracture segments

N_v' = Total number of nodes

y_{jc} = y coordinate of center point of the *j*-th fracture segment

SI Metric Conversion Factors

ft	×	3.048	e-01	=	m
ft^3	×	2.832	e-02	=	m^3
		(^{o}F-32)/1.8		=	^{o}C
cp	×	1.0	e-03	=	Pa·s
psi	×	6.895	e+00	=	kPa
md	×	1.0	e+15	=	m^2

References

Ajani, A., and Kelkar, M., 2012. Interference Study in Shale Plays. Presented at SPE Hydraulic Fracturing Technology Conference, 6-8 February, The Woodlands, Texas, USA. SPE 151045.

Awada, A., Santo, M., and Lougheed, D., 2016. Is That Interference? A Work Flow for Identifying and Analyzing Communication through Hydraulic Fractures in a Multi-Well Pad. SPE Journal, in press.

Cipolla, C.L., and Wallace, J., 2014. Stimulated Reservoir Volume: a Misapplied Concept? Presented at SPE Hydraulic Fracturing Technology Conference, 4-6 February, The Woodlands, Texas, USA. SPE 168596

CMG-IMEX. 2012. IMEX User's Guide, Computer Modeling Group Ltd.

Cohen, C.E., Xu, W., Weng, X., and Tardy, P.M.J., 2012. Production Forecast after Hydraulic Fracturing in Naturally Fractured Reservoirs: Coupling a Complex Fracturing Simulator and a Semi-Analytical Production Model. Presented at SPE Hydraulic Fracturing Technology Conference, 6-8 February, The Woodlands, Texas, USA. SPE 152541.

Gringarten, A.C., and Rameny, H.J.Jr., 1973. The Use of Source and Green's Functions in Solving Unsteady-Flow Problems in Reservoirs. SPE Journal 13 (5): 285-296.

Gringarten, A.C., Ramey, H.J.Jr., and Raghavan, R., 1972. Unsteady-State Pressure Distribution Created by a Well with a Single Infinite-Conductivity Vertical Fracture. SPE Journal 14 (4): 347-360.

Grossi, P., Neumann, D., and Lalehrokh, F., 2015. New Findings in Expected Ultimate Field Recoveries: Implications of Staggered Lateral Downspacing in the Eagle Ford Shale. Presented at Unconventional Resources Technology Conference, 20-22 July, San Antonio, Texas, USA. URTeC 2153935.

Guppy, K.H., Cinco-Ley, H., Ramey Jr., H.J., and Samaniego-V., F., 1982. Non-Darcy Flow in Wells with Finite-Conductivity Vertical Fractures. SPE Journal 22 (5): 681-698.

King, G.E., and Valencia, R.L., 2016. Well Integrity for Fracturing and Re-Fracturing: What is Needed and Why? Presented at SPE Hydraulic Fracturing Technology Conference, 9-11 February, The Woodlands, Texas, USA. SPE 179120.

Kurtoglu, B., and Salman, A., 2015. How to Utilize Hydraulic Fracture Interference to Improve Unconventional Development. Presented at International Petroleum Exhibition and Conference, 9-12 November, Abu Dhabi, UAE. SPE 177953.

Lawal, H., Jackson, G., Abolo, N., and Flores, C., 2013. A Novel Approach to Modeling and Forecasting Frac Hits in Shale Gas Wells. Presented at EAGE Annual Conference & Exhibition, 10-13 June, London, United Kingdom. SPE 164898.

Lehmann, J., Budge, J., Palghat, A., Petr, C., and Pyecroft, J., 2016. Expanding Interpretation of Interwell Connectivity and Reservoir Complexity through Pressure Hit Analysis and Microseismic Integration. Presented at SPE Hydraulic Fracturing Technology Conference, 9-11 February, The Woodlands, Texas, USA. SPE 179173.

Lindner, P. and Bello, H., 2015. Eagle Ford Well Spacing: A Methodology to Integrate, Analyze, and Visualize Multisource Data in Solving a Complex Value-Fouced Problem. Presented at Unconventional Resources Technology Conference, 20-22 July, San Antonio, Texas, USA. URTeC 2174709.

Malpani, R., Sinha, S., Charry, L., Sinosic, B., Clark, B., and Gakhar, K., 2015. Improving Hydrocarbon Recovery of Horizontal Shale Wells through Refracturing. Presented at SPE/CSUR Unconventional Resources Conference, Calgary, 20-22 October, Alberta, Canada. SPE 175920.

Marongiu-Porcu, M., Lee, D., Shan, D., and Morales, A., 2016. Advanced Modeling of Interwell-Fracturing Interference: An Eagle Ford Shale-Oil Study. SPE Journal, in press.

Olson, J.E., and Wu, K., 2012. Sequential versus Simultaneous Multi-zone Fracturing in Horizontal Wells: Insights from a Non-planar, Multi-frac Numerical Model. Presented at the SPE Hydraulic Fracturing Technology Conference, 6-8 February, The Woodlands, Texas, USA. SPE 152602.

Portis, D.H., Bello, H., Murray, M., Barzola, G., Clarke, P., and Canan, K., 2013. Searching for the Optimal Well Spacing in the Eagle Ford Shale: A Practical Tool-Kit. Presented at Unconventional Resources Technology Conference, 12-14 August, Denver, Colorado, USA. SPE-168810.

Potter, H.D.P., 2008. On Conformal Mappings and Vector Fields. Senior thesis, Marietta College, Marietta, Ohio.

Rimedio, M., Shannon, C., Monti, L., Lerza, A., Roberts, M., and Quiroga, J., 2015. Interference Behavior Analysis in Vaca Muerta Shale Oil Development, Loma Campana Field, Argentina. Presented at Unconventional Resources Technology Conference, 20-22 July, San Antonio, Texas, USA. SPE 178620.

Safari, R., Lewis, R., Ma, X., Mutlu, U., and Ghassemi, A., 2015. Fracture Curving Between Tightly Spaced Horizontal Wells. Presented at Unconventional Resources Technology Conference, 20-22 July, San Antonio, Texas, USA. URTeC 2149893.

Sani, A.M., Podhoretz, S.B., and Chambers, B.D., 2015. The Use of Completion Diagnostics in Haynesville Shale Horizontal Wells to Monitor Fracture Propagation, Well Communication, and Production Impact. Presented at SPE/CSUR Unconventional Resources Conference, 20-22 October, Calgary, Alberta, Canada. SPE 175917.

Sardinha, C., Petr, C., Lehmann, J., and Pyecroft, J., 2014. Determining Interwell Connectivity and Reservoir Complexity through Frac Pressure Hits and Production Interference Analysis. Presented at SPE/CSUR Unconventional Resources Conference, 30 September-2 October, Calgary, Alberta, Canada. SPE 171628.

Scott, K.D., Chu, W.C., and Flumerfelt, R.W., 2015. Application of Real-Time Bottom-Hole Pressure to Improve Field Development Strategies in the Midland Basin Wolfcamp Shale. Presented at Unconventional Resources Technology Conference, 20-22 July, San Antonio, Texas, USA. URTeC 2154675.

Sun, J., and Schechter, D., 2015. Optimization-Based Unstructured Meshing Algorithms for Simulation of Hydraulically and Naturally Fractured Reservoirs with Variable Distribution of Fracture Aperture, Spacing, Length, and Strike. SPE Reservoir Evaluation & Engineering 18 (4): 463-480.

Thambynayagam, R.M.K., 2011. The Diffusion Handbook: Applied Solutions for Engineers. New York: McGraw-Hill Professional.

Warpinski, N.R., Kramm, R.C., Heinze, J.R., and Waltman, C.K., 2005. Comparison of Single and Dual-Array Microseismic Mapping Techniques in the Barnett Shale. Presented at SPE Annual Technical Conference and Exhibition, 9-12 October, Dallas, Texas, USA. SPE 95568.

Weijermars, R., 1998. Principles of Rock Mechanics, 2nd edition, Alboran Science Publishing.

Weijermars, R., and Schmeling, H., 1986. Scaling of Newtonian and Non- Newtonian Fluid Dynamics without Inertia for Quantitative Modelling of Rock Flow Due to Gravity (Including the Concept of Rheological Similarity). Physics of the Earth and Planetary Interiors 43 (4): 316-330.

Weijermars, R., and van Harmelen, A., 2016. Breakdown Of Doublet Recirculation and Direct Line Drives by Far-Field Flow in Reservoirs: Implications for Geothermal and Hydrocarbon Well Placement. Geophysical Journal International 206: 19-47.

Weijermars, R., van Harmelen, A., Zuo, L., 2016. Controlling Flood Displacement Using a Parallel Analytical Streamline Simulator. Journal of Petroleum Science and Engineering 139: 23-42.

Wu, K. and Olson, J.E., 2016. Numerical Investigation of Complex Fracture Networks in Naturally Fractured Reservoirs. SPE Production & Operations, in press.

Wu, K., and Olson, J.E., 2013. Investigation of the Impact of Fracture Spacing and Fluid Properties for Interfering Simultaneously or Sequentially Generated Hydraulic Fractures. SPE Production and Operation 28 (4): 427-436.

Wu, K., and Olson, J.E., 2015a. Simultaneous Multi-Frac Treatments: Fully Coupled Fluid Flow and Fracture Mechanics for Horizontal Wells. SPE Journal 20 (2): 337-346.

Wu, K. and Olson, J.E., 2015b. A Simplified Three-Dimensional Displacement Discontinuity Method for Multiple Fracture Simulations. International Journal of Fracture 193 (2): 191-204.

Wu, R., Kresse, O., Weng, X., Cohen, C., and Gu, H., 2012. Modeling of Interaction of Hydraulic Fractures in Complex Fracture Networks. Presented at SPE Hydraulic Fracture Technology Conference, 6-8 February, The Woodlands, Texas, USA. SPE 152052.

Xu, G., and Wong, S.W., 2013. Interaction of Multiple Non-Planar Hydraulic Fractures in Horizontal Wells. Presented at International Petroleum Technology Conference, 26-28 March, Beijing, China. IPTC 17043.

Yaich, E., Diaz de Souza, O.C., Foster, R.A., 2014. A Methodology to Quantify the Impact of Well Interference and Optimize Well Spacing in the Marcellus Shale. Presented at SPE/CSUR Unconventional Resources Conference, 30 September-2 October, Calgary, Alberta, Canada. SPE 171578.

Yu, W., 2015. A Comprehensive Model for Simulation of Gas Transport in Shale Formation with Complex Hydraulic Fracture Geometry. Presented at SPE Annual Technical Conference and Exhibition, 28-30 September, Houston, Texas, USA. SPE 178747.

Yu, W., Sepehrnoori, K., and Patzek, T.W., 2016b. Modeling Gas Adsorption in Marcellus Shale with Langmuir and BET Isotherms. SPE Journal 21 (2): 589-600.

Yu, W., Wu, K., and Sepehrnoori, K., 2016a. A Semianalytical Model for Production Simulation from Nonplanar Hydraulic-Fracture Geometry in Tight Oil Reservoirs. SPE Journal 21 (3): 1028-1040.

Zhou, W., Banerjee, R., Poe, B., Spath, J., and Thambynayagam, M., 2013. Semianalytical Production Simulation of Complex Hydraulic-Fracture Networks. SPE Journal 19 (1): 6-18.

Appendix A: Analytical Drainage Model and Scaling Rules

A1-Analytical drainage model

The complex potential $\Omega(z)$ for an interval-source with non-dimensional strength [$m^*(t^*)$ positive for a line source; negative for a sink] along the real axis with the real interval $[a,b]$ is (Potter 2008):

$$\Omega(z)=\frac{m^*(t^*)}{b-a}\left[(z-a)\log(z-a)-(z-b)\log(z-b)\right]. \quad \text{(A-1)}$$

The corresponding velocity potential is $V(z)$:

$$V(z)=\frac{m^*(t^*)}{b-a}\left[\log(z-a)-\log(z-b)\right]. \quad \text{(A-2)}$$

The field $V(z)$ for a general interval-source located on the interval $[z_a, z_b]$ between $z_a(=a+i\cdot c)$ and $z_b(=b+i\cdot d)$ is (Weijermars and van Harmelen 2016):

$$V(z)=\frac{m^*(t^*)}{z_b-z_a}\left[\log(z-z_a)-\log(z-z_b)\right]. \tag{A-3}$$

Non-dimensional strengths in the 2D analytical drainage model, $m^*(t^*)$, relates to the volumetric flux, $Q^*(t^*)$, as follows:

$$Q^*\left(t^*\right) = m^*\left(t^*\right)\ 2\pi h_0{}^*. \tag{A-4}$$

where $h_0{}^*$ is the non-dimensional unit depth.

Eq. (A-3) can be rewritten as:

$$V(z)=\frac{m^*_{n}(t^*)}{b_n-a_n}e^{-i\beta_n}\left\{\log\left[e^{-i\beta_n}(z-z_{cn})-a_n\right]-\log\left[e^{-i\beta_n}(z-z_{cn})-b_n\right]\right\}, \tag{A-5}$$

where z_c is the centre of the interval-source and β_n is the angle that the interval-source makes with the x-direction and *n* is the number of fractures (**Figure A-1**). Eq. (A-5) can be applied to string together multiple line segments into any arbitrary fracture network. The velocities (u_x, u_y) of all fluid particles are found from:

$$V_z = u_x - iu_y. \tag{A-6}$$

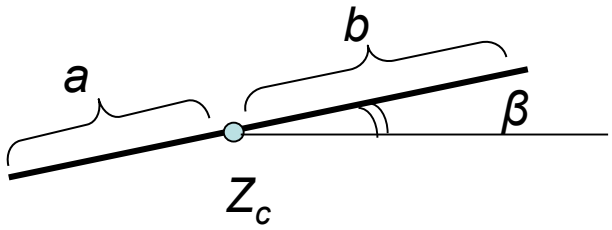

Figure A-1. Fracture element at location z_c.

Coding was completed in Matlab and results were validated against independent, ECLIPSE based streamlines simulations (Weijermars et al. 2016).

A2-Scaling rules

The reservoir simulator used to provide inputs for the analytical drainage simulator typically uses dimensional units whereas the analytical simulator typically uses non-dimensional units. Dimensional analysis can be applied to relate the dimensional quantities of the prototype reservoir to the non-dimensional quantities of the analytical drainage visualization model (Weijermars and Schmeling 1986; Weijermars et al. 2016). The drainage model must retain geometric and kinematic similarity with the prototype reservoir. These conditions will be fulfilled if the ratio of any model-prototype pairs of lengths and velocities remain identical. The fracture network lengths, $L_{X,Y}$, in the dimensional prototype can be normalized into a non-dimensional length units, $L^*_{X,Y}$, using the dimensional unit length, L_0, of the prototype as follows:

$$L^*_{X,Y} = L_{X,Y} / L_0. \tag{A-6}$$

Unlike length [*L*] and time [*T*], which are fundamental physical quantities, velocity is a derived physical quantity with dimension [LT^{-1}] (Weijermars 1998, Chapter 2), which therefore needs not be scaled independently for kinematic similarity. Time for flow in a fluid continuum (non-porous media) can be commonly scaled as:

$$t^* = t / t_0 . \quad \text{(A-7)}$$

However, the flux from the matrix into each fracture segment in the prototype reservoir is a porous medium where fluid is drained from a specific volume, V_s, as a fraction of the bulk unit rock volume, V_0, given by the effective porosity, ϕ:

$$\phi = V_s / V_0 . \quad \text{(A-8)}$$

Because the analytical model has effective porosity $\phi = 1$, time of flight in the analytical model will be proportionally longer than in the prototype reservoir when the latter has $\phi < 1$ (and velocity of fluid particle will be correspondingly slower in model as compared to prototype), which can be simply adjusted by scaling time as follows:

$$t^* = t / \left(\phi t_0 \right) . \quad \text{(A-9)}$$

The fluxes specified for the prototype reservoir model account for all reservoir parameters, such as fracture geometries, fracture conductivities, matrix permeability and well spacing.

In order to avoid overly complex re-adjustments between non-dimensional and dimensional time scales of respectively model and reservoir prototype, it is important to scale the analytical model directly with the appropriate fluxes, while ensuring correct geometric scaling.

We used a simple case with single planar fracture to demonstrate the combination of semi-analytical model and analytical streamline model to visualize the drainage area. The fracture and reservoir properties are the same as in Table 1. The single fracture was equally divided into 6 segments. The BHP is held at 3,000 psi for the simulation. In the analytical model, we scaled the reservoir model with geometric similarity to the semi-analytical prototype with length ratios 1:1. In this case, the strength (ft^2/day) of each line source will be given by:

$$m(t^*) = \frac{5.6145 Q(t)}{2\pi\phi h}, \quad \text{(A-10)}$$

where $Q(t)$ is the dimensional flux (bbl/day), ϕ is the matrix porosity, h is the respective depth of each fracture (ft), and 5.6145 is the flux conversion factor from bbl/day to scf/day. In the semi-analytical model the flux output is for unit height, so the respective depth $h = 1$ ft. Applying the above scaling formula, we can get Table A-1 for the flux strength scaling. We can see that $Q(t) = 1$ bbl/day corresponds to $m = 12.77$ ft^2/day. Under this scaling principle, the dimensional time t is equal to the dimensionless time $t*$.

Table A-1: Flux strength scaling

Properties	Value	Unit
Dimensional flux (Q)	1	bbl/day
Porosity (ϕ)	7%	-
Dimensional depth (h)	1	ft
Dimensional strength (m)	12.77	ft^2/day

Figure A-2 first compares the gas flow rate between the semi-analytical model and numerical model, illustrating that a good match was obtained. The oil flux for 3 segments of one fracture wing from the fracture tip to the wellbore is presented in **Figure A-3**. The others remain the same as these three segments due to the symmetric fracture geometry.

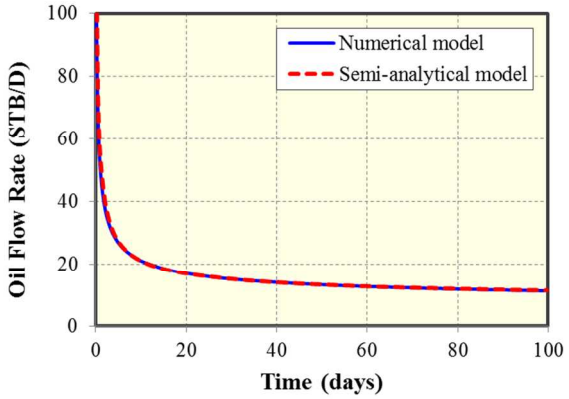

Figure A-2. Comparison of oil flow rate between the semi-analytical model and numerical model.

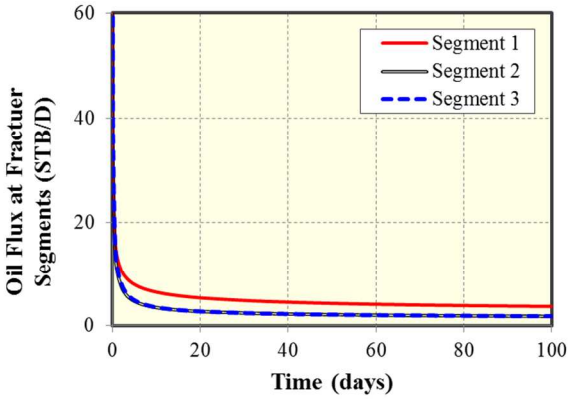

Figure A-3. Oil flux for 3 segments of one fracture wing from the fracture tip to the wellbore.

The pressure distribution after 30 days is shown in **Figure A-4**. After that, we used the oil flow flux from each fracture segment in the analytical streamline model. **Figure A-5** visualizes the corresponding advance of the drainage area, where the blue lines are the streamlines trajectories and the red lines are time of flight contours spaced for 30 days. Total drainage area shown is for 300 days of production.

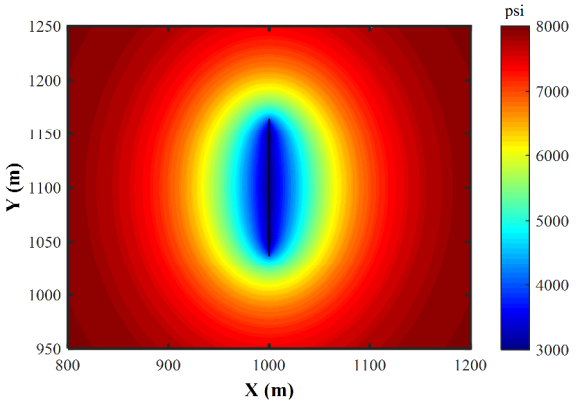

Figure A-4. Pressure distribution after 30 days of production for single planar fracture.

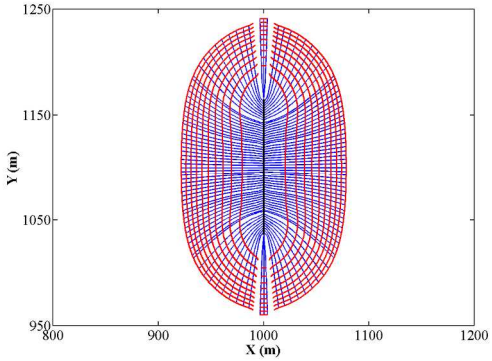

Figure A-5. Streamlines trajectories in blue and time of flight contours in red for the geometry in Figure A-4.

Appendix B: Two Extreme Case Studies

For the scenario of well interference through single slanted fracture hit, we performed two additional extreme case studies. Case 1 is with the highest conductivity of 100 md-ft for both connecting fracture and primary fracture and the lowest matrix permeability of 0.001 md. Case 2 is with the lowest conductivity of 0.1 md-ft for both connecting fracture and primary fracture and the highest matrix permeability of 0.1 md. The other fracture and reservoir properties remain the same as Table 1. **Figure B-1** compares the BHP of Well 1 for both cases. As shown, there is almost no detectable pressure response of shut-in well for Case 2 while there is a big pressure drop for Case 1. It confirms that larger fracture conductivity and smaller matrix permeability, more severe well interference through fracture hit.

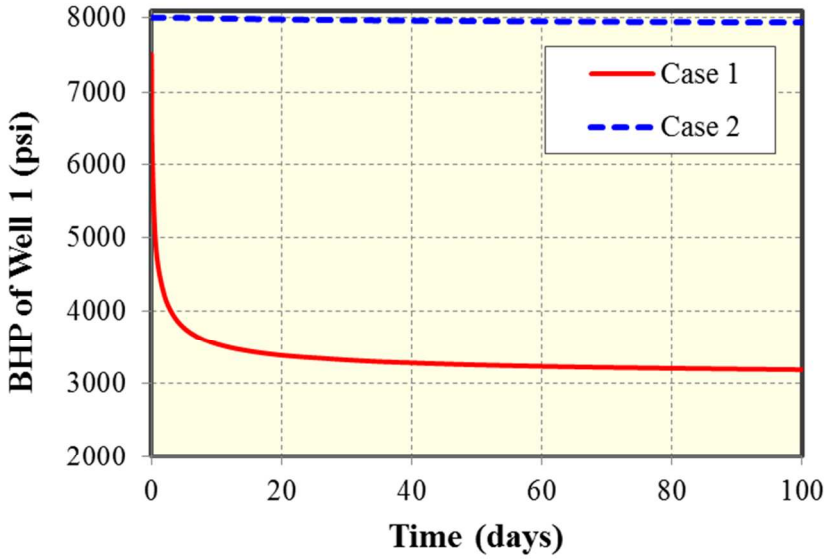

Figure B-1. Comparison of pressure response between two extreme cases for the scenario of well interference through single slanted fracture hit.